Unified Static–Dynamic Macro–Micro Robotic Palpation with Multi-actuation for Viscoelastic Property Mapping

Chongxun Wang[1], Harrison Teng[1], Qilin He[1], Nat Hsu[1], Lillian Chin[2] and Fangzhou Xia[1*]

Abstract— **Robotic palpation offers a more repeatable, quantitative touch-based assessment beyond subjective human examination. However, robotic palpation remains constrained by a fundamental tradeoff between large-workspace exploration and high-bandwidth contact interaction. We overcome this limitation by combining industrial robotic positioning with localized voice-coil actuation for multi-actuation macro–micro robotic palpation. A robot arm provides global surface coverage, while a directly mounted voice coil actuator (VCA) enables high-resolution quasi-static indentation and dynamic frequency sweep excitation with synchronized force and displacement sensing. We model this framework, linking indentation-derived stiffness to frequency-domain system identification and enabling decomposition of effective mass, stiffness, and damping during contact. We verify this model through one-dimensional phantom experiments, seeing a clear measured stiffness difference between solid, hollow and rigid insert samples. We further demonstrate the power of this approach by conducting two-dimensional phantom experiments on a soft surface with embedded air channels. We demonstrate a robust linear relationship between internal channel pressure and applied probing force ($R^2 \approx 0.99$). These results establish that our hybrid VCA-robot arm method provides spatial stiffness measurements that reliably resolve subsurface features.**

I. Introduction

Manual palpation is a standard procedure in clinical practice for identifying subsurface anomalies in soft tissue. Localized stiff regions and abnormal compliance may be signs of tumors, cysts, fibrotic lesions or hernia [1,2]. Clinicians rely on hand touching to infer internal structure from surface deformation, but this process is inherently subjective and dependent on individual experience, applied force, and probing strategy. As a result, manual palpation is difficult to standardize across practitioners and sessions, limiting its reproducibility and its suitability for longitudinal monitoring or algorithmic interpretation [3,4].

Robotic palpation offers a quantitative and repeatable alternative by enabling controlled indentation trajectories and consistent force application, producing measurements that can be directly compared across locations, trials, and subjects. Prior studies have shown that robotic palpation can achieve sensitivity comparable to or exceeding that of human assessment under controlled conditions [5], and that autonomous probing can be combined with machine learning to identify inclusions and estimate subsurface properties [6–8]. Robotic palpation can be classified by motion types into two categories: (1) quasi-static indentation methods, which relate applied force to measured displacement [9,10], and (2) dynamic motion with frequency domain techniques, which estimate viscoelastic parameters through dynamic indentation procedures [11,12].

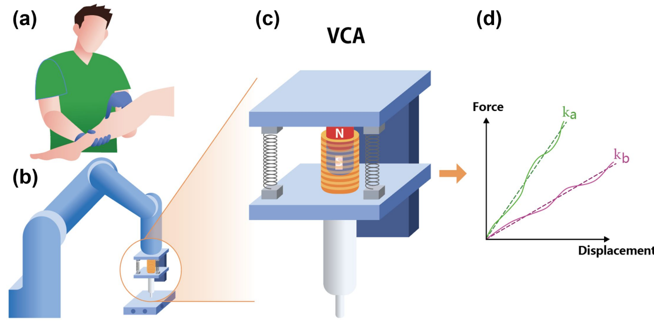

Fig. 1. To achieve a replacement to (a) manual clinical palpation, we propose (b) a robotic palpation system that integrates a robot arm with (c) a voice-coil actuator (VCA). This combination enables both high-bandwidth frequency sweep excitation and quasi-static indentation for controlled force application over a large area. (d) Sample image of extracted stiffness from measured force-displacement responses from the VCA.

However, both of these methods suffer from the tradeoff between workspace and interaction bandwidth. Quasi-static methods tend to use industrial robotic arms, which offer large workspaces and precise positioning. However, their contact interaction bandwidth is limited by actuator inertia, joint compliance, and control constraints [13,14]. Conversely, high-bandwidth actuators used for frequency-based techniques are capable of resolving fine mechanical responses, but typically operate over limited strokes and are unsuitable for large-area exploration [15]. Similar workspace–bandwidth tradeoffs have motivated macro–micro actuation designs in other robotic contact applications, where large-range positioning is combined with a small-stroke, high-bandwidth end-effector to generate repeatable dynamic contact forces [16]. However, this design principle has not been fully explored for robotic palpation, where systems must cover extended tissue surfaces while performing localized high-bandwidth mechanical probing, despite prior studies repeatedly highlighting the need for architectures that satisfy these competing requirements [17,18].

In this work, we present a hybrid robotic palpation platform with a multi-actuation architecture to enable both macro-scale positioning and high-bandwidth contact interaction (Fig. 1). The system combines the large workspace and positioning accuracy of an industrial robotic arm with the fine, localized probing capability of a voice coil actuator (VCA). This enables both quasi-static force-displacement measurements and dynamic frequency sweep excitation to be performed at each probing location without sacrificing workspace coverage. By integrating static and dynamic probing within a single system, the platform directly addresses the workspace-bandwidth tradeoff that limits many existing robotic palpation approaches. Stiffness estimates obtained from the VCA's force-displacement measurements are used to infer spatial variations within the phantom.

The contributions of this paper are: (1) A hybrid macro–micro robotic palpation architecture that combines large-workspace positioning with high-bandwidth voice-coil actuation and synchronized force, displacement, and pressure sensing. (2) A multi-method experimental framework that unifies quasi-static stiffness mapping, dynamic frequency-based system identification, and embedded pressure sensing within a single robotic probing platform. (3) A physics-grounded modeling framework that links actuator dynamics, indentation-based contact linearization, and ideal-gas air channel compression, allowing decomposition of effective mass, stiffness, and damping contributions during probing.

II. System Design and Integration

This section presents the mechanical and electronic integration of the multiactuated macro–micro palpation system. A KUKA iiwa robotic arm provides large-workspace positioning, while a directly mounted voice coil actuator (VCA) delivers high-bandwidth force control and displacement sensing at the contact interface, enabling wide-area coverage without sacrificing probing fidelity.

A. VCA-Based High-Bandwidth Probing Module

Localized probing is performed using a cylindrical VCA (Thorlabs VC250) (Fig. 2). The VCA operates on a direct-drive electromagnetic principle in which the generated force is proportional to the applied coil current. The VC250 provides a nominal force constant of 3.84 N/A near mid-stroke, enabling direct force regulation through current control. Owing to magnetic field non-uniformity, the force constant decreases with displacement and reduces to approximately 2.918 N/A at 24 mm travel. In the assembled configuration, the permanent magnet is rigidly fixed to the robot-mounted structure, while the coil assembly is free to translate along the axial direction. Electrical characterization of the integrated actuator yielded a coil resistance of 5.8 Ω and an inductance of 2.07 mH, which are incorporated into the current-control design and dynamic modeling.

To ensure purely translational motion, the moving coil is mechanically guided using side-mounted linear sliders that suppress off-axis loading. Passive tension springs with a combined stiffness of $k_v = 0.0439\ \mathrm{N/mm}$ provide restoring force and define the intrinsic actuator stiffness used in the dynamic model. A 3D-printed hemispherical probing tip (radius $R = 2.5\ \mathrm{mm}$) is attached to the moving coil and establishes the spherical contact geometry assumed in the Hertzian contact formulation.

Relative displacement of the moving coil is measured using a linear magnetic encoder (POSIC ID1102L) mounted parallel to the actuation axis. The encoder provides real-time linear displacement signal at 1 μm resolution for contact detection, quasi-static indentation measurements, and dynamic frequency sweep experiments. Together, the direct-drive VCA actuation and encoder-based displacement sensing form the high-bandwidth contact module of the system, enabling precise force–displacement characterization while the robotic arm provides global positioning.

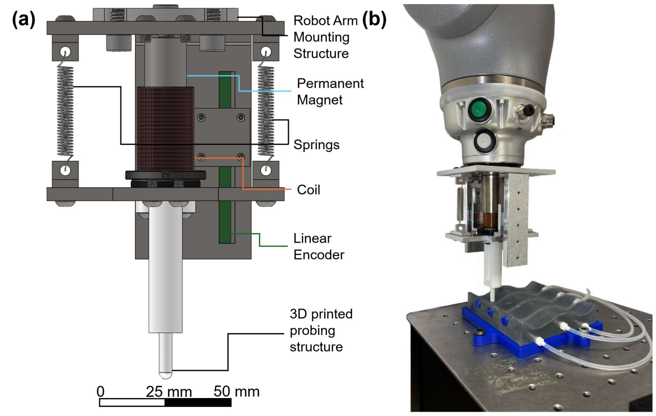

Fig. 2. Voice coil actuator (VCA) probing assembly. (a) CAD illustration of the VCA mounted to the robot end effector, showing the permanent magnet rigidly attached to the mounting structure, the translating coil guided by linear sliders, passive springs providing preload, and a linear encoder measuring relative displacement. (b) Photograph of the assembled probing system during a palpation experiment, illustrating the 3D-printed probing tip contacting a deformable test surface.

B. Robot Arm Integration and Real-Time Architecture

The VCA is mounted coaxially on an industrial Kuka iiwa robot arm as an end effector. The VCA is mounted to the robot arm's flange through a custom aluminum adapter plate. This plate maintains alignment of the actuation axis with the nominal surface normal. The robot arm is responsible for global positioning and surface tracing, like a macroscopic 3D profiler. During tracing, the robot moves laterally to prescribed locations and slowly advances along the z direction until surface contact is detected. Contact is detected via the VCA encoder. When a 200-count change (0.2 mm relative coil motion) is detected, motion is terminated and the 3D contact position is recorded.

The robot is commanded by a computer running the Sunrise Workbench environment. Meanwhile, VCA actuation and encoder sensing are handled by a second computer running LabVIEW, interfacing with a NI cRIO-9074 chassis. The VCA coil is driven by a NI 9505 DC motor drive module, while the linear encoder is sampled by the same NI 9505 module for displacement feedback. Synchronized operation is realized through network communication between the two computers implemented via TCP/IP. Encoder displacement values and system state information are exchanged to coordinate robot positioning and probing operations. This distributed architecture isolates deterministic current control and sensor acquisition from robot motion execution, while preserving flexible system-level coordination.

III. Dynamic Modeling of the System

This section develops a physics-based axial model of the coupled VCA–soft material system to enable parameter extraction from both quasi-static indentation and dynamic frequency-response measurements. The goal of the modeling framework is (i) to separate intrinsic actuator dynamics from

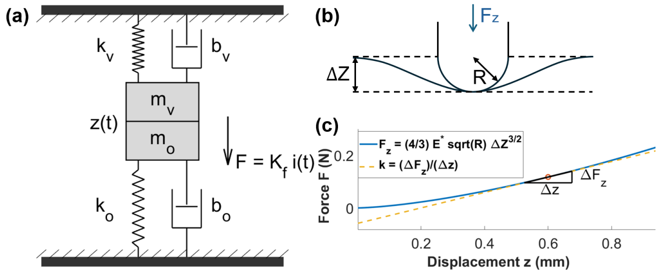

Fig. 3. Modeling framework for axial probing dynamics. (a) Lumped mass–spring–damper representation of the VCA assembly (m_v, k_v, b_v) in series with the contacted material (m_o, k_o, b_o), driven by electromagnetic force $F = K_f i(t)$. (b) Schematic of spherical indentation with probe radius R, indentation depth ΔZ, and normal contact force F_z used for Hertzian contact modeling. (c) Illustration of tangent stiffness extraction at an operating indentation depth from the force–displacement (F–z) curve, used for local linearization of the nonlinear contact response.

contact-induced effects, and (ii) to provide a unified representation that links static stiffness estimation with frequency-domain system identification. The probing dynamics are therefore modeled along the actuation axis as a single-degree-of-freedom (1-DOF) translational system. Because the probe tip is 3D-printed from PLA and is significantly stiffer than the soft material being palpated (Shore A hardness 28 and 50), the probe is treated as rigid, and all deformation during contact is assumed to occur within the soft material.

A. Free-Air Dynamics of the VCA Assembly

In free air, the moving assembly of the VCA is modeled as a lumped mass–spring–damper system (Fig. 3a):

$$m_v\ddot{z}(t) + b_v\dot{z}(t) + k_v z(t) = F(t),$$

where z is the VCA displacement, m_v is the effective moving mass, b_v is viscous damping, k_v is the combined stiffness of the return springs, and $F(t)$ is the electromagnetic actuation force, which is proportional to the input current $i(t)$:

$$F(t) = K_f \cdot i(t) = K_f \cdot (I_0 + I_a \sin(\omega t)),$$

where K_f is the actuator force constant and $i(t)$ is the coil current, separated into its DC and frequency components. The DC component $F_0 = K_f I_0$ produces static displacement and does not affect the small-signal natural frequency. The free-air dynamics are characterized by

$$\omega_{n,v} = \sqrt{\frac{k_v}{m_v}}, \qquad \zeta_v = \frac{b_v}{2\sqrt{k_v m_v}}.$$

Solving for the intrinsic inertial and damping properties of the VCA:

$$m_v = \frac{k_v}{\omega_{n,v}^2}, \qquad b_v = \frac{2\zeta_v k_v}{\omega_{n,v}}.$$

The free-air identification model establishes the intrinsic inertial and damping properties of the VCA assembly that we can use to isolate material-dependent dynamic contributions during contact.

B. Indentation-Based Contact Modeling

Now that we've established the VCA's intrinsics and force application $F(t)$, we can now derive the local contact stiffness k_o from quasi-static indentation experiments. During indentation, the total measured actuation force F is shared between the VCA return springs and the object. The force balance can therefore be written as $F = F_v + F_o$, where the VCA return spring force is $F_v = k_v \cdot \Delta Z$ and F_o is the object contact force associated with indentation depth ΔZ.

Two physical regimes may dominate the force–displacement response depending on internal structure. The first regime we model is the structural-deformation dominant regime. We expect to be in this regime when voids or geometric compliance provide a constant stiffness k. We can model this regime as a simple Hookean relationship: $F_o = k_o \cdot \Delta Z$.

The second regime we model is the contact-mechanics dominant regime. We expect to be in this regime when the material beneath the probe can be approximated as locally homogeneous. We choose to model this regime as Hertzian spherical contact (Fig. 3b), where the contact interaction is governed primarily by elastic deformation within a semi-infinite half-space. In this regime:

$$F_o = \frac{4}{3} E^* \sqrt{R}\, \Delta Z^{3/2},$$

where R is the radius of the hemispherical probe and E^* is the effective elastic modulus of the contacting bodies, defined as

$$\frac{1}{E^*} = \frac{1-\nu_o^2}{E_o} + \frac{1-\nu_p^2}{E_p},$$

where E_o, ν_o represent the Young's modulus and Poisson's ratio of the soft object, and E_p, ν_p represent those of the probe. Since the PLA probe is significantly stiffer than the soft object ($E_p \gg E_o$), the second term becomes negligible, and the effective modulus reduces to $E^* \approx \frac{E_o}{1-\nu_o^2}$.

In both of these models, the local tangent stiffness at operating displacement z_0 is calculated by

$$k_o(z_0) = \left.\frac{\partial F_o}{\partial z}\right|_{z=z_0} \tag{1}$$

Quasi-static indentation provides the local tangent stiffness $k_o(z)$ of the object response at the selected operating point (Fig. 3c), which is used as the contact stiffness term in the linearized dynamic model.

C. Contact Linearization and Effective Dynamics

To maintain continuous probe–object contact during dynamic excitation, the bias current satisfies

$$I_0 - I_a > I_c,$$

where I_c is the contact threshold current. Because

$$I_a \ll I_0 - I_c,$$

the nonlinear contact response can be linearized about operating depth z_0, and $k_o(z_0)$ is treated as a constant during frequency sweeps.

The contacted material is modeled locally as a Kelvin–Voigt element:

$$F_o = k_o z + b_o \dot{z},$$

where b_o represents viscoelastic damping.

Since both the VCA assembly and the contacted material contribute inertia, the effective moving mass becomes

$$m_{\text{eff}} = m_v + m_o,$$

where m_o is the effective inertia of the participating material.

The total contact dynamics are therefore

$$m_{\text{eff}}\ddot{z} + (b_v + b_o)\dot{z} + (k_v + k_o)z = K_f i(t).$$

The corresponding natural frequency and damping ratio under contact are

$$\omega_n = \sqrt{\frac{k_v + k_o}{m_{\text{eff}}}}, \qquad \zeta = \frac{b_v + b_o}{2\sqrt{(k_v + k_o)m_{\text{eff}}}}.$$

Under small-signal excitation, the probe–material interaction is approximated as a linear second-order system whose effective mass, stiffness, and damping reflect both actuator properties and local material behavior. This formulation enables dynamic parameter extraction from frequency response data.

IV. 1D Experimental Validation and Structural Characterization

This section presents controlled validation of the proposed robotic palpation framework using one-dimensional (1D) test objects with spatially varying internal structures. The objective of the 1D study is (i) to evaluate spatial stiffness estimation via quasi-static indentation, and (ii) to verify consistency between static stiffness trends and dynamic frequency-response identification.

Three 1D test objects were evaluated: *hollow*, *solid*, and *insert*. For each object, ten probing locations (Position 1–10) were selected evenly along the longitudinal axis of the surface, spaced 9 mm apart. The CAD renderings in Fig. 4(b) highlight the ten discrete indentation sites used for mechanical testing. This uniform spatial sampling ensures consistent coverage across the region of interest and enables direct comparison of mechanical responses at corresponding positions among the three configurations.

At every location, quasi-static indentation tests were performed. Dynamic frequency sweeps were conducted at Position 3, where structural differences among configurations are most pronounced.

A. Quasi-Static Indentation and Spatial Stiffness Mapping

Indentation was performed by incrementally increasing the VCA current by 0.01 A every 100 ms while recording the encoder displacement. Each location was tested five times to assess repeatability. The applied force was calculated using the actuator force constant $K_f = 2.918$ N/A, with the initial contact current $I_c = 0.5$ A used to remove preload effects.

For all quasi-static analyses, the force–displacement curves shown in Fig. 4(a) were averaged across trials, with variability indicated by error bars. The F_o–z curves represent the net object contact force, with the return spring force of VCA subtracted using the known spring stiffness k_v. Thus, the plotted F_o–z relationship corresponds to the net object response after removing the VCA return-spring contribution.

When the material beneath the probe can be approximated as locally homogeneous (e.g., the *solid* object, the *insert* object away from the inclusion, and the *hollow* object at non-void positions), the response is well described by a Hertzian contact model, consistent with indentation into an effectively uniform elastic medium. In contrast, when a void lies directly beneath the probe (notably Position 1–3 in the *hollow* configuration), the response is better approximated by a linear stiffness model, reflecting reduced structural support rather than classical Hertzian behavior.

The goodness-of-fit supports this interpretation. The Hertz model provides near-unity R^2 values for both the *solid* and *insert* configurations, indicating that their force–displacement responses are largely governed by contact mechanics. The fit is slightly stronger for the *solid* case than for the *insert* case ($R^2 = 0.99980$ vs. 0.99727), consistent with the assumption of material homogeneity underlying Hertz theory and the mild deviation introduced by the embedded inclusion.

For the *hollow* configuration at Position 3, where structural deformation dominates due to the underlying void, the linear model achieves an R^2 score of 0.99793, confirming that the response in this region is better described by structural compliance rather than Hertzian contact.

For coupling the quasi-static indentation results to the dynamic frequency-sweep model, a local tangent stiffness was extracted at the same bias condition used in the sweep experiments. The dynamic tests use a sinusoidal current input with a 1.0 A DC offset and 0.1 A amplitude; therefore, the operating point was selected at the bias current $I_0 = 1.0$ A. With the contact threshold current $I_c = 0.5$ A and actuator force constant $K_f = 2.918$ N/A, the corresponding object contact force is

$$F_0 = (I_0 - I_c)K_f = (1.0 - 0.5) \times 2.918 = 1.459 \text{ N}$$

The quasi-static tangent stiffness evaluated at this bias force was then used as the local linear stiffness in the second-order dynamic model. This operating-point formulation also remains consistent with manual palpation, where clinicians typically apply a probing force and infer internal structure from the resulting deformation.

For each configuration, the depth of the indentation z_0 corresponding to F_0 was obtained from the fitted model F_o - z plus the spring return forces. The local operating-point stiffness was then computed using the tangent stiffness definition in (1), evaluated at $z = z_0$.

The extracted indentation depths at Position 3 were:

- Insert: $z_0 = 2.314$ mm,
- Solid: $z_0 = 2.935$ mm,
- Hollow: $z_0 = 4.49$ mm.

The corresponding local operating-point tangent stiffness values were:

- Insert: $k_o = 0.94571$ N/mm,
- Solid: $k_o = 0.74555$ N/mm,
- Hollow: $k_o = 0.3249$ N/mm.

To obtain the effective stiffness used in dynamic modeling, the return spring stiffness was added back according to $k_{\text{eff}} = k_v + k_o$, consistent with the model described in Section III. Because this bias-force linearization leads to different equilibrium indentation depths across configurations, the extracted stiffness values should be interpreted as local operating-point tangent stiffnesses rather than intrinsic material stiffnesses evaluated at a common displacement. However, this operating-point variation does not account

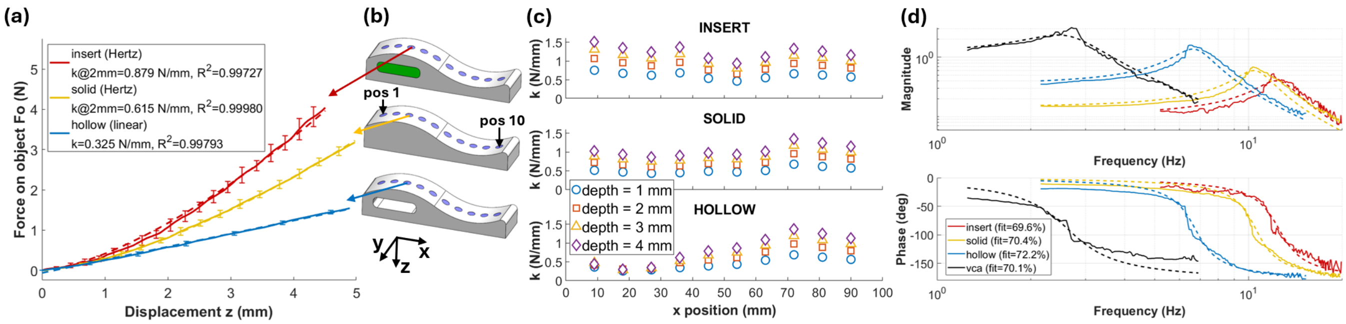

Fig. 4. 1D indentation and stiffness characterization. (a) Averaged force–displacement (F_o–z) curves for the hollow, solid, and insert configurations (mean ± s.d. $n = 5$). The hollow case is fitted with a linear model, while the solid and insert cases are fitted using a Hertzian contact model. (b) CAD models of the 1D test objects highlighting the ten probing positions along the surface. (c) Spatial stiffness values obtained from the slope of the F–z curves at different indentation depths, showing depth- and configuration-dependent mechanical variations. (d) Frequency sweep responses of the insert, solid, hollow configurations at Position 3, and the standalone VCA actuator. Measured magnitude (top) and phase (bottom) are shown together with their corresponding second-order system identification fits, highlighting configuration-dependent dynamic characteristics and actuator dynamics.

for the observed stiffness ordering. As shown by the full $F_o - z$ curves in Fig. 4(a), the insert, solid, and hollow configurations exhibit separated force–displacement trends over the measured displacement range.

Fig. 4(c) summarizes the spatial stiffness computed from the local slope of the fitted F_o–z curves at indentation depths of 1 mm, 2 mm, 3 mm, and 4 mm. Distinct spatial patterns emerge across configurations. In the *hollow* object, Positions 1–3 exhibit consistently low stiffness values that remain nearly uniform across indentation depths, indicating deformation dominated by the underlying void rather than depth-dependent contact mechanics. In contrast, Positions 1–4 in the *insert* configuration show higher stiffness than the same positions in the *solid* configuration, which in turn exceeds the *hollow* configuration, reflecting the increasing structural support provided by the embedded rigid inclusion.

Across Positions 6–10, where no void or inclusion lies beneath the probe, stiffness values converge across configurations. Position 8 consistently exhibits the highest stiffness, corresponding to the thinnest local material region and reduced compliance. Overall, the spatial ordering of stiffness—insert > solid > hollow at structurally distinct locations—matches the expected internal geometry. These results indicate that quasi-static stiffness estimation alone provides a reliable and physically interpretable measure of internal structural variation.

B. Dynamic Frequency Sweep and System Identification

Dynamic characterization was performed using sinusoidal current sweep to extract the frequency response. The VCA current was driven by a sinusoidal signal with a 1.0 A DC offset and 0.1 A amplitude. The excitation frequency was swept from 2 Hz to 20 Hz in 0.05 Hz increments. At each frequency, steady-state magnitude and phase responses were recorded and aggregated into a frequency response function.

Assuming force input and displacement output, the contacted probe–material system is modeled as a linear second-order system:

$$G(s) = \frac{Z(s)}{F(s)} = \frac{1}{m_{\text{eff}} s^2 + b_{\text{eff}} s + k_{\text{eff}}}, \tag{2}$$

where m_{eff}, b_{eff}, and k_{eff} denote the effective mass, damping, and stiffness of the total system under contact.

Rewriting (2) in normalized second-order form yields

$$G(s) = \frac{1/m_{\text{eff}}}{s^2 + 2\zeta\omega_n s + \omega_n^2},$$

where

$$\omega_n = \sqrt{\frac{k_{\text{eff}}}{m_{\text{eff}}}}, \qquad \zeta = \frac{b_{\text{eff}}}{2\sqrt{k_{\text{eff}} m_{\text{eff}}}}.$$

The effective stiffness k_{eff} used in this dynamic analysis was obtained independently from quasi-static indentation, where $k_{\text{eff}} = k_v + k_o$ was evaluated at the same bias-force operating point as the dynamic sweep.

1) Free-Air Identification (VCA Baseline): Prior to contact experiments, the VCA assembly was characterized in free air. The identified parameters were

$$\omega_{n,v} = 16.5192 \text{ rad/s } (2.629 \text{ Hz}), \qquad \zeta_v = 0.2595.$$

Using the known spring stiffness $k_v = 0.0439$ N/mm, the effective moving mass and damping of the VCA assembly were obtained as

$$m_v \approx 161 \text{ g}, \qquad b_v \approx 1.38 \text{ N s/m}.$$

The identified mass closely matches the measured moving assembly mass of 161 g, validating the modeling framework and system identification procedure.

2) Contact Identification: Dynamic identification was performed at Position 3 for the *insert*, *solid*, and *hollow* configurations under continuous contact. The identified natural frequencies were:

- Insert: $\omega_n = 78.673$ rad/s (12.52 Hz),
- Solid: $\omega_n = 66.3066$ rad/s (10.55 Hz),
- Hollow: $\omega_n = 42.3921$ rad/s (6.75 Hz).

This ordering of natural frequencies for three configurations, insert > solid > hollow, is consistent with the static stiffness trends extracted from quasi-static indentation. Since the natural frequency scales with $\omega_n = \sqrt{(k_v + k_o)/m_{\text{eff}}}$, configurations with higher effective stiffness are expected to exhibit higher resonance frequencies.

Using

$$m_{\text{eff}} = \frac{k_{\text{eff}}}{\omega_n^2},$$

with k_{eff} determined from the previous subsection, the effective moving masses were computed as:

- Insert: $m_{\text{eff}} \approx 160$ g,
- Solid: $m_{\text{eff}} \approx 179$ g,

- Hollow: $m_{\text{eff}} \approx 205$ g.

The solid and insert case yields an effective mass nearly identical to the free-air VCA mass, indicating minimal additional inertial contribution from the inclusion. In contrast, the hollow cases exhibit larger apparent effective masses, reflecting increased material participation in oscillatory motion and deviation from ideal small-signal linearization in more compliant regions.

The identified damping ratios were:

- Insert: $\zeta = 0.1375$,
- Solid: $\zeta = 0.1258$,
- Hollow: $\zeta = 0.1330$.

Material damping contributions were extracted by subtracting the baseline VCA damping, yielding:

- Insert: $b_o \approx 0.80$ N s/m,
- Solid: $b_o \approx 1.58$ N s/m,
- Hollow: $b_o \approx 0.97$ N s/m.

Although the natural frequencies exhibit a clear monotonic ordering consistent with stiffness trends, the identified damping ratios are comparatively similar across configurations. This indicates that resonance frequency is primarily governed by effective stiffness rather than damping variations in the present system.

C. Consistency between two methods

Taken together, the quasi-static stiffness ordering and the dynamic resonance trends exhibit strong agreement. The consistent relationship between k_o, k_{eff}, and ω_n confirms that the static indentation-based stiffness estimates directly govern the dynamic frequency response. This cross-method consistency validates the proposed modeling framework and demonstrates that both time-domain and frequency-domain measurements capture the same underlying structural variations within the test objects.

V. 2D Experimental Spatial Stiffness Mapping and Subsurface Void Detection

The indentation-based stiffness framework is extended to a two-dimensional (2D) soft pad with embedded air channels (Fig. 5). In contrast to the 1D validation study, the 2D experiment integrates embedded pressure sensing to evaluate subsurface cavity participation. The goal is to assess depth-dependent stiffness sensitivity and to determine how pneumatic feedback complements mechanical mapping.

A. Experimental Setup and Sensing Integration

A $90\,\text{mm} \times 100\,\text{mm}$ pad is 3D printed using Formlabs Elastic 50A resin and contains six embedded air channels (diameter $5\,\text{mm}$): three shallow wave-like channels conforming to the top surface profile and three deeper cylindrical channels. Each channel is connected to an ELVH-L05D-HRRD-I-NAA4 differential pressure transducer. Pressure signals are acquired using a NI 9205 module on the same NI cRIO-9074 chassis used for VCA control, enabling synchronized acquisition of current (contact force), displacement, and multi-channel pressure signals.

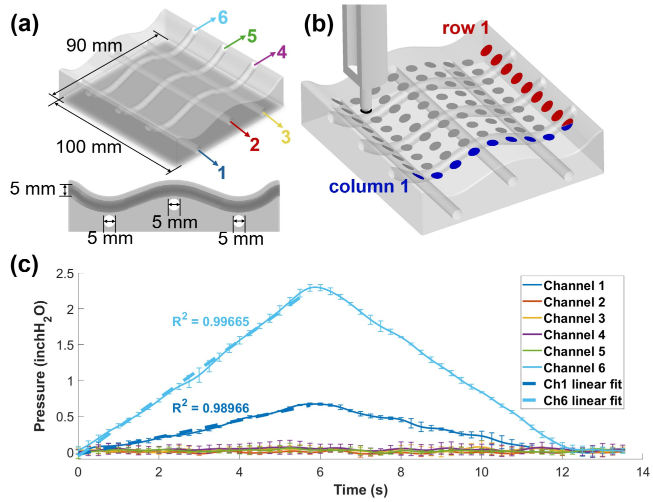

Fig. 5. 2D soft pad with embedded air channels and representative pressure response. (a) $90\,\text{mm} \times 100\,\text{mm}$ pad fabricated using Formlabs Elastic 50A resin, containing six embedded air channels (channels 4-6 shallower and channels 1-3 deeper), each connected to a differential pressure transducer. All the channels have a diameter of $5\,\text{mm}$. (b) 9×9 indentation grid used for stiffness mapping; the first row (red) and first column (blue) are highlighted. The shown probing point (row 8, column 8) lies directly above top channel 6 and bottom channel 1. (c) Pressure responses (mean $\pm$ s.d., $n = 3$) during indentation at row 8, column 8. The VCA current is ramped from 0.5 A to 3 A and back, producing monotonic loading and unloading. Channels 1 and 6 exhibit linear pressure–force behavior with $R^2 = 0.98966$ and $R^2 = 0.99665$, respectively, indicating proportionality between channel pressure and applied probing force.

A 9×9 indentation grid is defined over the top surface (Fig. 5 b). At each grid location, quasi-static indentation is performed three times by increasing the VCA current in 0.01A increments every 25ms and then symmetrically decreasing it to complete the unloading phase. The excitation spans from 0.5A (contact threshold) to 3A, generating a monotonic loading–unloading cycle.

B. Row-wise Force–Displacement Characterization

To examine spatial trends, we first analyze the force–displacement (F_o–z) responses along row 3 (Fig. 6(a)), highlighted by the black rectangular box in Fig. 6(b). This row was selected because it contains grid points directly above the shallow channels as well as neighboring grid points not directly above shallow channels. Meanwhile, all points along this row are located above the deeper channel layer, making the deeper-channel contribution relatively consistent across the row. Therefore, stiffness differences along row 3 primarily reflect the local influence of the shallow channels.

The nine grid points along this row exhibit two distinct stiffness groups. Columns 2, 5, and 8 display consistently lower slopes compared to the remaining columns. These locations correspond to probing directly above the shallow air channels (Channels 4–6). In contrast, columns 1, 3, 4, 6, 7, and 9 are not directly above shallow channels and exhibit higher effective stiffness. Because the deeper channel layer is present beneath all points along this row, this row-wise comparison suggests that the observed stiffness reduction is dominated by the shallow channels rather than by variations in the deeper layer.

Both linear and Hertz contact models were fitted to the F_o–z curves. Across all nine positions, the linear model

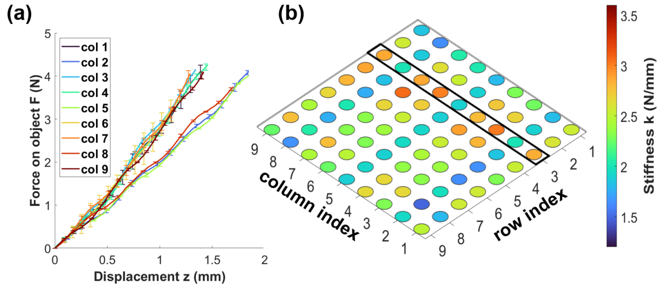

Fig. 6. 2D stiffness characterization and model comparison. (a) Force–displacement responses (mean ± s.d., $n = 3$) for all nine grid points along row 3 (black rectangle in (b)). Columns 2, 5, and 8 exhibit lower slopes than the remaining columns, corresponding to probing directly above the shallow air channels (Channels 4–6). (b) Spatial stiffness map over the 9×9 grid, where stiffness is evaluated as $k_o = (F_o(0.75) - F_o(0.25))/0.5\,\mathrm{mm}$. Points in columns 2, 5, and 8 show consistently lower stiffness, indicating reduced resistance above shallow cavities. In contrast, locations aligned with the deeper channel layer show weaker stiffness contrast, indicating limited sensitivity to deeper subsurface structures under the available probing force.

TABLE I

R^2 COMPARISON BETWEEN LINEAR AND HERTZ MODELS FOR ROW 3.

	C1	C2	C3	C4	C5	C6	C7	C8	C9
Linear	0.994	0.996	0.994	0.993	0.996	0.996	0.992	0.997	0.994
Hertz	0.975	0.957	0.970	0.974	0.957	0.974	0.968	0.941	0.975

achieves higher R^2 values than the Hertz model (Table I), even at locations without a directly underlying shallow cavity. This indicates that under the present geometric and loading conditions, a linear stiffness descriptor more robustly characterizes local response than idealized Hertzian contact.

C. 2D Stiffness Map Construction

Given the consistently superior linear fits, stiffness is computed using a finite-difference approximation of the local slope:

$$k_o = \frac{F_o(0.75\,\mathrm{mm}) - F_o(0.25\,\mathrm{mm})}{0.5\,\mathrm{mm}}.$$

The resulting 9×9 stiffness map (Fig. 6(b)) clearly delineates the shallow channels (columns 2, 5, 8), while rows aligned with deeper channels show minimal contrast.

These results indicate reliable detection of cavities at approximately $5\,\mathrm{mm}$ depth, with substantially reduced sensitivity beyond $10\,\mathrm{mm}$. The limited depth sensitivity arises from the stiffness of the 50A resin and the finite probing force of the VCA, which restrict stress propagation into deeper layers.

D. Air Channel Pressure Response and Volume Compression

During indentation at row 8, column 8, channel pressure increases approximately linearly with applied contact force. Linear regression yields $R^2 = 0.99665$ (shallow) and $R^2 = 0.98966$ (deeper), with no significant hysteresis during the unloading trajectory.

The proportional behavior suggests that pressure sensing can serve as a quantitative indicator of probing force during indentation.

To relate pressure rise to volumetric change, the enclosed air in each channel–tube assembly is modeled as an ideal gas undergoing isothermal compression during slow indentation, such that Boyle's law applies:

$$P_1 V_1 = P_2 V_2,$$

where P_1 is ambient pressure (101,325 Pa), and V_1 is the total enclosed volume including the embedded channel and the connected plastic tube. Each channel has diameter $5\,\mathrm{mm}$ ($r = 2.5\,\mathrm{mm}$). The shallow channels have effective lengths of $90\,\mathrm{mm}$ and the deeper channels $100\,\mathrm{mm}$. The connected tube has inner diameter $1/16\,\mathrm{in}$ and length $50\,\mathrm{cm}$. The resulting enclosed volumes are:

$$V_{1,\mathrm{top}} \approx 2757\,\mathrm{mm}^3, \qquad V_{1,\mathrm{bottom}} \approx 2953\,\mathrm{mm}^3.$$

During indentation, the shallow channel exhibits a pressure increase of $2.3\,\mathrm{inH_2O}$ ($\approx 573\,\mathrm{Pa}$), while the deeper channel shows $0.67\,\mathrm{inH_2O}$ ($\approx 167\,\mathrm{Pa}$). Using Boyle's law,

$$\frac{\Delta V}{V_1} = 1 - \frac{P_1}{P_2}, \qquad P_2 = P_1 + \Delta P,$$

the volumetric changes are estimated as:

$$\Delta V_{\mathrm{top}} \approx 15.5\,\mathrm{mm}^3, \qquad \Delta V_{\mathrm{bottom}} \approx 4.85\,\mathrm{mm}^3.$$

The shallow channel undergoes roughly three times the volumetric compression of the deeper channel.

Meanwhile, if the measured $3\,\mathrm{mm}$ probing-structure displacement recorded by the encoder were assumed to translate entirely into cavity collapse of the top channel, the ideal compressed volume would be

$$\Delta V_{\mathrm{ideal}} \approx 35.57\,\mathrm{mm}^3,$$

whereas the measured total compression is

$$\Delta V_{\mathrm{measured}} \approx 20.35\,\mathrm{mm}^3.$$

This discrepancy indicates that the collapse of the embedded channel is partial rather than complete, with deformation distributed within the surrounding resin. The deeper channel shows a smaller deformation, consistent with the reduced pressure rise observed experimentally.

E. 2D Experiments Result Discussion

The 2D experiments reveal three key characteristics of indentation-based spatial stiffness mapping.

First, quasi-static stiffness mapping reliably detects shallow cavities from the air channel but exhibits limited sensitivity to deeper structures. Mechanical coupling decreases rapidly with depth due to material stiffness (shore hardness of 50A) and finite probing force (approximately 7-8 N). This behavior is consistent with manual palpation, where superficial anomalies are more readily detected than deeply embedded lesions.

Second, pressure sensing provides a robust and repeatable linear pressure–force relationship across both shallow and deeper channels with near-unity R^2 values when pressure is regressed against contact force.

Ideal-gas modeling provides a quantitative interpretation of the measured pressure rise. Under a perfectly compliant geometric assumption, $3\,\mathrm{mm}$ indentation would yield approximately $35.57\,\mathrm{mm}^3$ of channel compression, whereas the pressure-derived estimate is approximately $20.35\,\mathrm{mm}^3$. This gap indicates partial collapse of the embedded air channels, with a significant portion of deformation distributed within the surrounding material. The shallow channel exhibits roughly three times the volumetric change of the deeper channel, confirming stronger mechanical coupling to near-surface cavities.

Third, the Hertz contact model does not outperform a linear model in the 2D setting. This can be attributed to three factors: (i) indentation is applied along the z axis while the surface is non-planar, resulting in non-normal contact conditions; (ii) the limited indentation range produces an approximately linear force–displacement response within the sampled window; and (iii) the embedded channel network introduces spatial heterogeneity that violates classical Hertz assumptions. These factors make linear slope-based stiffness more stable and interpretable for spatial mapping.

Together, these results demonstrate that shallow structure anomalies can be identified through stiffness mapping, while proportional pneumatic pressure sensing feedback provides complementary force-dependent information. The combined mechanical–pneumatic framework offers a physically interpretable approach for subsurface detection under realistic material and geometric constraints.

VI. Conclusion and Future Work

This work presented a hybrid macro–micro robotic palpation framework that decouples large-workspace positioning from high-bandwidth contact interaction. By integrating a KUKA iiwa arm with a directly mounted voice coil actuator (VCA), the system enables unified quasi-static indentation and dynamic frequency sweep excitation.

The 1D study demonstrated strong static-dynamic consistency between indentation-derived stiffness and dynamic system identification, with stiffness ordering (insert $>$ solid $>$ hollow) directly reflected in resonance frequencies. The 2D experiments extended this framework to spatial stiffness mapping and embedded air channel pressure sensing. Quasi-static stiffness can reliably identify shallow cavities from the channel, while depth sensitivity decreased with increasing material thickness, due to material stiffness and limited probing force. Air-channel pressure exhibited a robust linear relationship with applied probing force, which can be used as a stable proportional indicator of probing force. Together, stiffness mapping and linear pneumatic sensing offer complementary, physically interpretable modalities for characterizing internal structure in soft materials.

Future work will focus on improving depth sensitivity and geometric consistency through surface-normal estimation, adaptive probing strategies, and higher-force excitation within actuator limits, enabling more accurate normal indentation and enhanced detection of deeper structures. Finite element analysis (FEA) of nonlinear material behavior and channel deformation will be incorporated to quantify stress transmission beyond idealized Hertzian or linear contact assumptions. In parallel, data-driven inversion methods will be explored to select or blend contact models automatically and to map quasi-static, dynamic, and pressure-response features to subsurface material fields without requiring prior knowledge of the underlying structure. The framework will also be extended to anatomically realistic, multi-layered, and anisotropic phantoms with more complex internal topologies to evaluate robustness under conditions closer to biological tissue.

References

[1] L. Bickley and P. G. Szilagyi, *Bates' guide to physical examination and history-taking*. Lippincott Williams & Wilkins, 2012.

[2] N. J. Talley and S. O'connor, *Clinical examination: a systematic guide to physical diagnosis*. Elsevier Australia, 2010.

[3] J. Ophir, I. Cespedes, H. Ponnekanti, Y. Yazdi, and X. Li, "Elastography: a quantitative method for imaging the elasticity of biological tissues," *Ultrasonic imaging*, vol. 13, no. 2, pp. 111–134, 1991.

[4] R. Sinkus, M. Tanter, T. Xydeas, S. Catheline, J. Bercoff, and M. Fink, "Viscoelastic shear properties of in vivo breast lesions measured by mr elastography," *Magnetic resonance imaging*, vol. 23, no. 2, pp. 159–165, 2005.

[5] J. C. Gwilliam, Z. Pezzementi, E. Jantho, A. M. Okamura, and S. Hsiao, "Human vs. robotic tactile sensing: Detecting lumps in soft tissue," in *2010 IEEE haptics symposium*. IEEE, 2010, pp. 21–28.

[6] K. A. Nichols and A. M. Okamura, "Autonomous robotic palpation: Machine learning techniques to identify hard inclusions in soft tissues," in *2013 IEEE International Conference on Robotics and Automation*. IEEE, 2013, pp. 4384–4389.

[7] B. Xiao, W. Xu, J. Guo, H.-K. Lam, G. Jia, W. Hong, and H. Ren, "Depth estimation of hard inclusions in soft tissue by autonomous robotic palpation using deep recurrent neural network," *IEEE Transactions on Automation Science and Engineering*, vol. 17, no. 4, pp. 1791–1799, 2020.

[8] Y.-j. Lee, S.-w. Bang, J.-b. Hong, and S. Park, "Image-free tumor segmentation of soft tissue using a minimally invasive robotic palpation system," *IEEE Transactions on Biomedical Engineering*, 2025.

[9] M. Griffin, Y. Premakumar, A. Seifalian, P. E. Butler, and M. Szarko, "Biomechanical characterization of human soft tissues using indentation and tensile testing," *Journal of visualized experiments: JoVE*, no. 118, p. 54872, 2016.

[10] Z. Wang, K. Kadoma, and S. Hirai, "An indentation-type instrument for measuring soft tissue elasticity," in *International Conference on Innovation in Medicine and Healthcare*. Springer, 2017, pp. 121–129.

[11] H. Koruk, S. B. Yurdaer, H. O. Koc, and A. Besli, "Identification of the viscoelastic properties of soft materials using a convenient dynamic indentation system and procedure," *Materials Today: Proceedings*, vol. 57, pp. 464–468, 2022.

[12] M. U. Ozcan, S. Ocal, C. Basdogan, G. Dogusoy, and Y. Tokat, "Characterization of frequency-dependent material properties of human liver and its pathologies using an impact hammer," *Medical Image Analysis*, vol. 15, no. 1, pp. 45–52, 2011.

[13] N. Hogan, "Impedance control: An approach to manipulation: Part ii—implementation," *Journal of dynamic systems, measurement, and control*, vol. 107, no. 1, pp. 8–16, 1985.

[14] A. Sharon, N. Hogan, and D. E. Hardt, "High bandwidth force regulation and inertia reduction using a macro/micro manipulator system," in *Proceedings. 1988 IEEE International Conference on Robotics and Automation*. IEEE, 1988, pp. 126–132.

[15] S. Haddadin, A. De Luca, and A. Albu-Schäffer, "Robot collisions: A survey on detection, isolation, and identification," *IEEE Transactions on Robotics*, vol. 33, no. 6, pp. 1292–1312, 2017.

[16] Y. F. Yeung, F. Xia, J. Covarrubias, M. Furokawa, T. Hirano, and K. Youcef-Toumi, "Robotic method and instrument to efficiently synthesize faulty conditions and mass-produce faulty-conditioned data for rotary machines," in *2023 IEEE International Conference on Robotics and Automation (ICRA)*. IEEE, 2023, pp. 11 382–11 388.

[17] J. Konstantinova, A. Jiang, K. Althoefer, P. Dasgupta, and T. Nanayakkara, "Implementation of tactile sensing for palpation in robot-assisted minimally invasive surgery: A review," *IEEE Sensors Journal*, vol. 14, no. 8, pp. 2490–2501, 2014.

[18] F. Chikweto, "Development of a robotic palpation sensor system for prostate cancer screening," Ph.D. dissertation, Tohoku University, 2016.